BIOCHEMISTRY
including biophysical chemistry & molecular biology
Article

*Biochemistry* **2009,** *48,* 5263–5275 5263
DOI: 10.1021/bi900584q

# The Myosin C-Loop Is an Allosteric Actin Contact Sensor in Actomyosin[†]

Katalin Ajtai,[‡] Miriam F. Halstead,[‡] Miklós Nyitrai,[⊥] Alan R. Penheiter,[§] Ye Zheng,[‡] and Thomas P. Burghardt*[,‡,∥]

[‡]*Biochemistry and Molecular Biology and* [§]*Molecular Medicine Program and* [∥]*Physiology and Biomedical Engineering, Mayo Clinic College of Medicine, Rochester, Minnesota 55905, and* [⊥]*Department of Biophysics, University of Pécs, Pécs, Hungary*

*Received April 6, 2009; Revised Manuscript Received April 30, 2009*

ABSTRACT: Actin and myosin form the molecular motor in muscle. Myosin is the enzyme performing ATP hydrolysis under the allosteric control of actin such that actin binding initiates product release and force generation in the myosin power stroke. Non-equilibrium Monte Carlo molecular dynamics simulation of the power stroke suggested that a structured surface loop on myosin, the C-loop, is the actin contact sensor initiating actin activation of the myosin ATPase. Previous experimental work demonstrated C-loop binds actin and established the forward and reverse allosteric link between the C-loop and the myosin active site. Here, smooth muscle heavy meromyosin C-loop chimeras were constructed with skeletal (sCl) and cardiac (cCl) myosin C-loops substituted for the native sequence. In both cases, actin-activated ATPase inhibition is indicated mainly by the lower $V_{max}$. In vitro motility was also inhibited in the chimeras. Motility data were collected as a function of myosin surface density, with unregulated actin, and with skeletal and cardiac isoforms of tropomyosin-bound actin for the wild type, cCl, and sCl. Slow and fast subpopulations of myosin velocities in the wild-type species were discovered and represent geometrically unfavorable and favorable actomyosin interactions, respectively. Unfavorable interactions are detected at all surface densities tested. Favorable interactions are more probable at higher myosin surface densities. Cardiac tropomyosin-bound actin promotes the favorable actomyosin interactions by lowering the inhibiting geometrical constraint barriers with a structural effect on actin. Neither higher surface density nor cardiac tropomyosin-bound actin can accelerate motility velocity in cCl or sCl, suggesting the element initiating maximal myosin activation by actin resides in the C-loop.

Myosin is an actin-dependent molecular motor driving sarcomeric shortening and muscle contraction by transducing ATP hydrolysis free energy into directed protein movement (*1*). ATP hydrolysis is coupled to a series of conformational changes in myosin, which result in a cycle of attachment to the actin filament, strain development, protein translation, actin release, and reattachment (*2*). Myosin conformation change associated with strain development and protein translation, termed the power stroke, is shown in crystal structures by a lever arm rotation through ~70° (*3*, *4*).

Myosin heavy chain (MHC)[1] is a linear molecule consisting of an N-terminal globular head domain called subfragment 1 (S1) and a C-terminal tail responsible for cargo binding or dimerization. Elliptically shaped S1 (~130 Å × 70 Å) contains subdomains referring to proteolytic fragments (25, 50, and 20 kDa) (*5*) or functional domains (*6*). Functional domains retain their structure, but move relatively, during transduction. Transduction starts in the active site with ATP hydrolysis. A long α-helical switch 2 helix transmits linear force originating from the active site to a converter domain converting linear force into torque to rotate the lever arm. The lever arm is another long α-helix stabilized by bound myosin light chains. The lever arm amplifies displacement and impels myosin relative to actin (*7*, *8*).

Multiple peptides within the 50K portion of S1 constitute the actin binding site. Protein−protein contacts in actomyosin were identified by experimental structural studies combined with simulated docking of the myosin and actin crystal structures (*9*−*13*), via detection of changes in actin binding strength, actin-activated myosin ATPase, and in vitro motility caused by the mutation of small peptide segments or individual residues in myosin (*14*−*16*). Primary hydrophobic actin contacts are helical segments, amino acids 529−558[2] and 647−659, on S1, while the

[†]This work was supported by NIH-NIAMS Grant R01AR049277, Mayo Clinic, and by Hungarian Science Foundation OTKA Grant K60968 to M.Ny.

*To whom correspondence should be addressed. Telephone: (507) 284-8120. Fax: (507) 284-9349. E-mail: burghardt@mayo.edu.

[1]Abbreviations: *β*S1, *β*-cardiac myosin subfragment 1; C-loop, loop 4 of amino acids 362−376; cCl, cardiac C-loop smooth muscle myosin chimera; Dc, *Dictyostelium discoideum*; Δ*G*, Δ*H*, and Δ*S*, change in free energy, enthalpy, and entropy, respectively; DOF, degree of freedom; ELC, essential light chain; HCTm, human cardiac tropomyosin; HMM, heavy meromyosin; mATP and mADP, fluorescent nucleotides mant-ATP and mant-ADP, respectively; MHC, myosin heavy chain; MLCK, myosin light chain kinase; MCMD, Monte Carlo molecular dynamics; PAGE, polyacrylamide gel electrophoresis; PMSF, phenylmethanesulfonyl fluoride; Rh, rhodamine; RLC, regulatory light chain; S1, myosin subfragment 1; sCl, skeletal C-loop smooth muscle myosin chimera; SKTm, rabbit skeletal tropomyosin; Tm, tropomyosin; U50a or U50b, myosin skeletal sequence of amino acids 145−361 or 362−462, respectively; W510, nucleotide sensitive tryptophan; WT, wild-type isoform.

[2]All myosin residue numbering uses the skeletal sequence unless noted otherwise.

 Published on Web 05/01/2009 

unstructured surface loop 2 (amino acids 626−647) maintains ionic interactions with the actin N-terminus. Secondary sites are an unstructured surface loop (amino acids 567−578) and the structured myopathy loop (amino acids 404−415) (*9*) also on the S1 surface.

Experimental work comparing the tertiary structure of skeletal and β-cardiac MHC identified a structured loop on the cardiac S1 (βS1) surface (amino acids 362−376), called the cardiac loop or C-loop, that has an influence on active site coupling to actin and possibly a direct interaction with actin (*17*). Limited proteolysis of skeletal S1 cleaves the heavy chain at loop 1 (amino acids 202−217) and loop 2, producing 25, 50, and 20 kDa molecular mass fragments (*5*). These loops are involved in regulation of substrate release (loop 1) and in actin binding and regulation of actin-activated ATPase (loop 2) (*14*, *18*). Limited proteolysis of βS1 cleaves the heavy chain at equivalent points and at the C-loop within the 50 kDa fragment. We found that C-loop cleavage affects βS1 $Mg^{2+}$ATPase, suggesting it participates in energy transduction (*17*). Actin binding protected loop 2 from proteolysis in skeletal S1, indicating the involvement of loop 2 in actin binding (*19*, *20*). Actin binding to βS1 fails to inhibit loop 2 cleavage (*21*) but does inhibit C-loop cleavage (*17*). These observations indicated skeletal and βS1 differ in conformation and identified the C-loop as a possible actin binding site. The C-loop was proposed as a site of actin binding in skeletal S1 (*12*, *13*), in myosin V (*22*), and in myosin I where it is called loop 4 (*23*).

The two proteolytic cutting points in skeletal S1 are within unstructured surface loops. Structured surface loops have also figured in myosin motor function. The myopathy loop is a structured surface loop containing an unusual clustering of mutations implicated in heart disease (*15*, *24*). The myopathy loop is an actin binding site (*9*, *12*), and the role of its point mutations implicated in disease in motor functions was thoroughly investigated (*15*, *25*, *26*). The C-loop is another structured surface loop adjacent to the myopathy loop (*17*). It begins at a highly conserved G362 at the end of a helix−turn−helix segment originating from the active site. The C-loop connects to the myopathy loop via a small helix−turn−helix segment containing several mutations implicated in heart disease (*24*). The crystallized myosin isoforms have differing detailed C-loop structure, although all are qualitatively similar in appearance except for a class I myosin, *Dictyostelium discoideum* (Dc) MyoE, where the C-loop is larger (*23*).

The crystal structure of Dc MyoE has a loop 4 longer by several residues than that in class II βS1. It was suggested loop 4 interferes with binding of MyoE to actin when regulatory proteins are present (*23*). Actin with bound tropomyosin had inhibited Myo1b (another class I myosin with a long loop 4) motor activity compared to a mutant version in which loop 4 was truncated or substituted with a shorter loop 4 from Dc myosin II (*27*). WT Myo1b actin motility was technically unmeasurable in the presence of tropomyosin; however, bare actin motility showed loop 4 mutation increased actin velocity. A loop 4 mutant in Dc myosin II confirmed its actin binding function and suggested loss of actin-activated ATPase function (*28*).

We constructed smooth muscle myosin mutants by substituting single amino acids or whole C-loop sequences from βS1 and skeletal S1 to investigate how sequence perturbs C-loop function. ATPase, actin-activated ATPase, active site kinetics, actin binding, and in vitro motility functional tests demonstrate the C-loop plays the central role in mediating active site and actin-binding site communication. These data, together with previous results from nonequilibrium Monte Carlo molecular dynamics (MCMD) simulation elucidating allosteric activation by actin of myosin ATPase (*29*), suggest that the C-loop is the sensor that when perturbed by actin binding commits myosin to ATP turn over. MCMD simulation suggests the mechanism for commitment to ATP turnover is the simultaneous conformation transition in the two myosin domains spanned by the C-loop to lower the entropic barrier to hydrolysis product release.

## EXPERIMENTAL PROCEDURES

*Chemicals*. Ammonium sulfate, ATP, ADP, sodium azide, dimethylformamide (DMF), dithiothreitol (DTT), phenylmethanesulfonyl fluoride (PMSF), and β-D-(+)-glucose were from Sigma (St. Louis, MO). Phalloidin and pyrene iodoacetamide were from Molecular Probes (Eugene, OR). The Bradford protein concentration assay was from Bio-Rad (Hercules, CA). Leupeptin, chymostatin, and pepstatin were from Roche Applied Sciences (Indianapolis, IN). Ni-NTA agarose was from Qiagen (Valencia, CA). Hexokinase was from Worthington Biochemical Corp. (Lakewood, NJ). All chemicals were reagent grade or Ultra-Pure if available.

*Cloning, Mutagenesis, Expression, and Purification of Smooth Muscle Myosin Light Chain Kinase (MLCK)*. The short smooth muscle variant of MLCK (isoform 5) was obtained from a human MLCK full-length cDNA clone (a generous gift from A. Bresnick, Albert Einstein College of Medicine, New York, NY) by PCR. The primers used were FWD 5′-GCA CCA TGG CTC ATC ATC ATC ATC ATC ACG ATT TCC CTG CCA ACC TGC-3′ and REV 5′-CCT CTA GAA ATA TGA CTT AGA AAC TGC. The FWD primer includes a minimal N-terminal six-histidine encoding sequence, while the REV primer contains an XbaI restriction site. The PCR product was subcloned into pCRBluntII-Topo (Invitrogen, Carlsbad, CA), and the smMLCK encoding insert was excised with NdeI and XbaI and inserted into NdeI- and XbaI-digested pVL1392 baculovirus transfer vector. Sf9 cells were transfected with pVL1392:smMLCK and Sapphire baculovirus DNA (Orbigen, San Diego, CA) to create a recombinant baculovirus expressing smMCLK, and the virus was amplified to a titer of $2 \times 10^8$ per milliliter. For recombinant protein production, $5 \times 10^8$ Sf9 cells were infected with a multiplicity of infection of 5 for 48 h at 28 °C. Cells were pelleted by centrifugation and frozen at −80 °C. MLCK was purified using the method of Birukov et al. (*30*) with modifications. Cell pellets were lysed in a 1:5 weight:volume ratio of 50 mM Tris (pH 8.5), 100 mM KCl, 10 mM 2-mercaptoethanol, 1% IGEPAL (octylphenyl-polyethylene glycol), 1 mM PMSF, 0.01 mg/mL pepstatin, and 0.01 mg/mL chymostatin, at 4 °C for 30 min. The lysate was centrifuged at 10000*g* for 30 min, and the supernatant was loaded onto 0.5 mM Ni-NTA, washed with 10 mL of 20 mM Tris (pH 8.5), 500 mM KCl, 5 mM 2-mercaptoethanol, and 1 mM PMSF in 10% glycerol, and eluted with 20 mM Tris (pH 8.5), 100 mM KCl, 5 mM 2-mercaptoethanol, 1 mM PMSF, and 100 mM imidazole in 10% glycerol. The eluate buffer was exchanged into 20 mM Tris (pH 7.5), 100 mM KCl, 10 mM DTT, and 5% sucrose. The MLCK was stored at −80 °C. The protein concentration was measured by using an $A_{278}$ of 11.4 and a molecular mass of 130 kDa. Baculovirus stocks for MLCK constructs were made at the Baculovirus/Monoclonal Antibody Core, Dan L. Duncan Cancer Center at Baylor College of Medicine (Houston, TX). Protein expressions were also carried out at this facility.

Table 1: C-Loop and Myopathy Loop Sequences[a]

| **Table 1.** C-loop and Myopathy loop sequences [a] | | |
|---|---|---|
| Myosin isoform | C-loop (362-376) | Myopathy loop (404-417) |
| Skeletal | **G**NLK**F**----KQKQREEQAE | PRVKV**G**----NEFVTKGQ |
| βS1 | **G**NMK**F**----KLKQREEQAE | PRVKV**G**----NEYVTKGQ |
| Scallop | **G**EMK**F**----KQRPREEQAE | PRVKV**G**----TEMVTKGQ |
| Smooth | **G**NIV**F**----KKERNTDQAS | PRIKV**G**----RDVVQKAQ |
| Dc II | **G**NIK**F**----EKGAGEGAVL | PRILA**G**----RDLVAQHL |
| Dc IE | **G**NIT**F**AEAAEQRTGTTTVK | RSIST**G**VGKRCSVISVPM |
| Smooth muscle myosin mutants | | |
| G362A | A**N**IV**F**----KKERNTDQAS | PRIKV**G**----RDVVQKAQ |
| G409V | **G**NIV**F**----KKERNTDQAS | PRIKV**V**----RDVVQKAQ |
| cCl | **G**NIV**F**----KLKQREEQAS | PRIKV**G**----RDVVQKAQ |
| sCl | **G**NIV**F**----KQKQREEQAS | PRIKV**G**----RDVVQKAQ |

[a] Myosin sequences for several isoforms with highly conserved residues are shown with bold text. Mutations introduced into the smooth muscle myosin isoform and tested for functionality are underlined in the bottom portion.

*Cloning, Mutagenesis, and Expression of Chicken Gizzard HMM*. A pFastBac construct plasmid containing cDNA of a recombined WT chicken gizzard smooth muscle HMM heavy chain was a gift from H. Onishi (Japan Sci/Tech Agency, Sayo, Hyogo, Japan). Recombinant HMM MHC has a myc tag at its C-terminus and a His tag at its N-terminus as described previously (*31*). Recombinant HMM heavy chain mutants, G362A, G409V, cCl, and sCl, were produced by replacing the WT MHC residue or C-loop with Ala, Val, human cardiac C-loop, and human skeletal C-loop, respectively. Table 1 compares C-loop and myopathy loop sequences for several myosin isoforms and the sequences for the mutants constructed.

The pFastBac constructs were transformed into *Escherichia coli* XL10 Gold cells (Stratagene, Santa Clara, CA) for production of the pFastBac construct plasmid DNA. The purified pFastBac construct plasmids were further transformed into DH10Bac *E. coli* for transposition into the bacmids. After confirming that the recombinant bacmids contained the gene of interest, we purified the recombinant bacmids and used them to transfect Sf9 insect cells to produce recombinant baculovirus. Sf9 cells were coinfected with equal titers of the MHC encoding baculovirus and a baculovirus encoding WT RLC and ELC. Construction of baculovirus stocks and protein expression was accomplished by the Baculovirus/Monoclonal Antibody Core.

*Protein Purification*. Wild-type and mutant HMMs were purified as described by Onishi et al. (*32*). On average, 1−2 mg of protein was purified from $1 \times 10^9$ cells. Protein purity ranged from 90 to 98%. Expressed protein samples are shown in Figure 1 using 12% SDS−PAGE. The eluted sample was treated with 5 mM EDTA to remove residual bound nucleotide and precipitated in a dialysis solution of 25 mM TES (pH 7.0), 1 mM EDTA, 5 mM DTT, and 1 μg/mL leupeptin containing 85% ammonium sulfate. The precipitate was collected via centrifugation and stored at −20 °C for 2−6 months with no loss of specific activity. Proteins for experiment were dialyzed in assay buffers overnight to remove ammonium sulfate and EDTA.

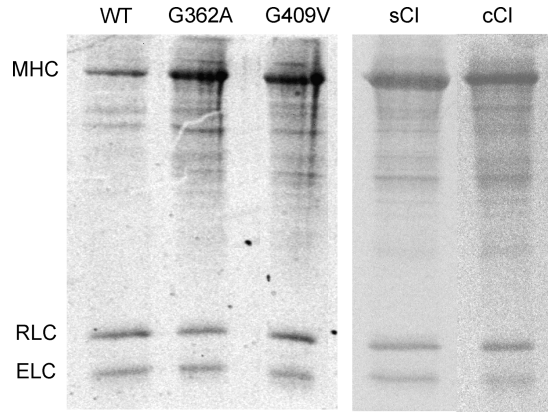


FIGURE 1: SDS−PAGE of WT HMM, mutants G362A and G409V, and chimeras containing skeletal (sCl) and β-cardiac (cCl) C-loop sequences. The myosin heavy chain (MHC) and light chains (RLC and ELC) correspond to molecular masses of 140, 20, and 17 kDa, respectively.

Skeletal actin was prepared from rabbit skeletal muscle acetone dried powder according to the method of Pardee and Spudich (*33*).

Protein concentrations were estimated by using the Bradford assay with bovine serum albumin as the protein standard.

*ATPase- and Actin-Activated ATPase Assays*. $K^+$-EDTA-ATPase activity was measured on samples at 37 °C in 250 μL aliquots containing 0.15−0.30 μM expressed HMM, 0.6 M KCl, 10 mM EDTA, 25 mM Tris-HCl (pH 8.0), and 2 mM ATP. The $Ca^{2+}$ATPase assay test solution was identical to that of $K^+$EDTA-ATPase except 10 mM $CaCl_2$ replaced the EDTA. Production of inorganic phosphate from the ATPase reaction was measured using the Fiske-Subbarow method (*34*).

$Mg^{2+}$ATPase and actin-activated $Mg^{2+}$ATPase activities were measured on samples at 25 °C in 300 μL volumes containing 0.23 μM expressed HMM, 30 mM KCl, 2 mM $MgCl_2$, 0.2 mM $CaCl_2$, 0.5 mM DTT, 30 mM Tris (pH 7.6), and 1 mM ATP. HMM was phosphorylated via addition of 40 μg/mL recombinant MLCK and 10 μg/mL bovine brain calmodulin to the assay medium 25 min prior to ATPase activity measurement. The kinase activity was stopped by adding 2 mM EGTA. RLC phosphorylation was 100% as estimated by urea gel electrophoresis (*35*). The actin concentration varied from 0 to 140 μM. Phosphorylated WT HMM exhibited ∼40-fold maximal actin activation.

Curves of $Mg^{2+}$ATPase rate versus actin concentration, [A], were evaluated with the equation $V = V_{max}/(1 + K_{ATPase}/[A])$ to obtain the apparent dissociation constant ($K_{ATPase}$) and maximum velocity ($V_{max}$). Baseline $Mg^{2+}$ATPase activity when [A] = 0 was subtracted from all data points. Production of inorganic phosphate from the ATPase reaction was measured using the malachite green assay (*36*). $Mg^{2+}$ATPase rate versus actin concentration data and curve fitting are discussed in the Supporting Information.

*Experiments with Pyrene-Labeled Actin*. Strong binding of myosin to actin was assessed in WT HMM and mutants using pyrene-labeled F-actin (p-F-actin). Pyrene fluorescence in p-F-actin is quenched by HMM binding. The actin binding assay used

phalloidin-stabilized p-F-actin (*37*). The labeling efficiency was 96%. Myosin binding was assessed using 0.2 $\mu$M actin in rigor or in the presence of 0.5 mM MgADP as described previously (*38*, *39*). The ADP stock solution was pretreated with 35 units of hexokinase and 10% glucose to remove ATP impurities. Measurements were taken at 20 °C in 25 mM Tris (pH 7.5), 0.1 M KCl, 2 mM $MgCl_2$, 1 mM DTT, and 1 $\mu$g/mL leupeptin. Reversibility of the actin binding was measured by adding 2 mM ATP to the sample after the binding measurements had been completed; 85−90% of the pyrene fluorescence intensity was recovered after ATP addition.

Scheme 1 describes the two-step binding of adjacent actin monomers ($A_2$) by the two-headed HMM ($M_2$) with one $M_2(1)$ or two $M_2(2)$ bound heads.

*Enzyme Kinetics*. Three recombinant HMMs were studied, WT, G362A, and G409V. They were prepared in Rochester and were not phosphorylated according to the urea gel PAGE analyses (*35*). In Pécs, the frozen, ammonium sulfate-precipitated samples were defrosted, dissolved in dialysis buffer consisting of 20 mM Tris-HCl (pH 7.5), 0.1 M KCl, 1 mM DTT, and 1 $\mu$g/mL leupeptin, and dialyzed. The HMM concentration was 1−5 $\mu$M as estimated by the Bradford assay. Experiments were conducted at 20 °C.

Rapid kinetic stopped-flow experiments were carried out on a temperature-controlled Applied Photophysics (Surrey, U.K.) stopped-flow instrument capable of recording light intensity changes on the millisecond time scale. Tryptophan fluorescence was measured with an excitation wavelength of 295 nm through emission filter WG320 passing wavelengths longer than 320 nm. The fluorescence transients obtained with p-F-actin (pyrene fluorescence) or with mant nucleotides were recorded using an excitation wavelength of 365 nm and emission through a KV389 high-pass filter passing wavelengths longer than 389 nm. Three to six transients were obtained and averaged before the analysis. The concentrations are given as they were established after the stopped-flow shots, unless stated otherwise.

*In Vitro Motility*. The gliding velocity of rhodamine-labeled phalloidin-F-actin (Rh-phalloidin-F-actin) over a bed of HMM was measured as described previously (*40*). Briefly, we removed "dead heads" by mixing phalloidin-actin with HMM, increasing the KCl concentration, adding ATP, and then spinning down the mixture in an airfuge. The supernatant contains the "live heads" that were phosphorylated. We checked RLC phosphorylation with urea gel PAGE (*35*). Glass coverslips coated with 1% nitrocellulose in amyl acetate formed the bottom of the flow cell. An anti-myc tag antibody solution was applied to the flow cell and allowed to equilibrate at room temperature. Myosin surface density was varied by flowing different antibody concentrations (0.15 or 0.35 mg/mL anti-myc flow-through) over the nitrocellulose-coated surface prior to addition of HMM. Blocking buffer (containing BSA) washed out unbound antibody and blocked protein free surface area. HMM was infused into the flow cell and equilibrated. Unbound HMM was removed by washing. Any remaining dead heads on the slide were blocked with phalloidin-F-actin that was subsequently removed from functioning heads by an ATP-containing wash. Rh-phalloidin-F-actin (2 nM) was added and allowed to equilibrate. Movement was initiated by adding 2 mM ATP at 20 °C. Actin sliding velocities were measured from acquired total internal reflection fluorescence (TIRF) images using NIH ImageJ with MTrack J Plugin written by E. Meijering. Computed velocities were plotted in histograms for actin velocity increment versus event count.

The sliding velocities of unregulated actin and actin with bound tropomyosin (Tm-actin) were tested. Tm-actin was prepared as described previously (*41*), where 100 nM Rh-phalloidin-F-actin was incubated with 200 nM Tm for 15 min at room temperature. The complex was diluted to 2 nM actin immediately before being added to the infusion cell. A total of 18 motility conditions consisting of low- and high-surface density WT-HMM, sCl, and cCl on actin and Tm-actin were tested, where Tm was rabbit skeletal (SKTm) or recombinant human cardiac (HCTm). The tropomyosins were a generous gift from D. Szczesna-Cordary (University of Miami, Miami, FL). HCTm has two additional amino acids (alanine and serine) at the N-terminus to mimic the acetylation needed for the biological activity. Motility data from cCl/HCTm-actin at low myosin surface density and cCl/SKTm-actin at high myosin surface density and both myosin surface densities for sCl/SKTm-actin were sampled insufficiently to provide statistics, leaving 14 conditions undergoing the global analysis described in Results.

Stoichiometric actin−Tm binding was verified from samples pelleted in the ultracentrifuge and then run on an SDS−PAGE gel. Gel densitometry of Coomassie-stained bands showed an ~5:1 actin:Tm coiled coil dimer ratio.

*MCMD Simulation of Myosin*. The dominant kinetic pathway for the actomyosin ATPase cycle is summarized in Scheme 2. where M, M*, M**, and M^ are intermediates corresponding to distinct myosin conformations, A is actin, T is ATP, D is ADP, and P is inorganic phosphate. M* and M** weakly bind actin, while M and M^ strongly bind actin. Work production occurs when M** weakly binds actin, forming a strong actin bond in M^ and inducing the active site "back door" (Arg245−Gln468 salt bridge) to open to release product P (*42*). The lever arm rotates to impel actin, ending in the low-free energy rigor state A.M. Cross-bridge repriming begins with ATP binding to A.M initiating dissociation from actin, hydrolysis of ATP, and reversal of the lever arm power stroke rotation. The power stroke, envisioned by comparison of the M** and M crystal structures, rotates the lever arm through ~70° (*3*, *4*). We performed a dynamics simulation for myosin joining the known M** and M transient intermediate structures in the Scheme 2 pathway using a nonequilibrium Monte Carlo molecular dynamics (MCMD) simulation of the M** → M conformation trajectory (*29*).

The lever arm swing conformation change in myosin occurs on the millisecond time domain and involves many atoms. We developed the new dynamics simulation strategy because system complexity excludes use of standard molecular dynamics methods. Myosin was partitioned into gear peptides [from the cog and gear analogy of Geeves and Holmes (*43*)] that undergo dynamics in small backbone dihedral angle changes (each changing parameter is a degree of freedom or DOF) and block domains that

Scheme 1

$$A_2 + M_2 \overset{K_{A1}}{\leftrightarrow} A_2 \cdot M_2(1) \overset{K_{A2}}{\leftrightarrow} A_2 \cdot M_2(2)$$

Scheme 2

$$\begin{array}{ccccc} A\cdot M + T & \longleftrightarrow & A\cdot M^{*}\cdot T & \qquad & A\cdot M^{**}\cdot D\cdot P \longleftrightarrow A\cdot M^{\wedge}\cdot D \longleftrightarrow A\cdot M \\ & & \updownarrow & & \updownarrow \\ & & M^{*}\cdot T & \longleftrightarrow & M^{**}\cdot D\cdot P \end{array}$$

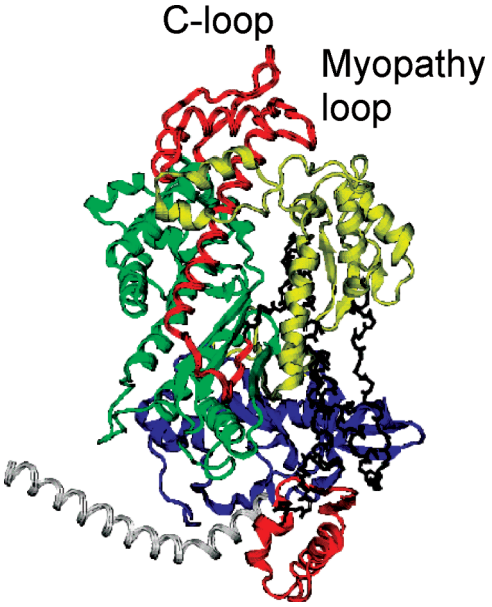


FIGURE 2: Domain-partitioned S1 heavy chain in the M** conformation. S1 has block peptides designated N-terminal (amino acids 1−144, blue ribbon), U50a (amino acids 145−361, green ribbon), U50b (amino acids 362−462, red tube, top), loop 2 containing (amino acids 526−695, yellow ribbon), converter (amino acids 721−772, red ribbon, bottom), and lever arm (amino acids 773−812, white ribbon). Gear peptides are amino acids 463−525 and 696−720 (black stick backbone bonds).

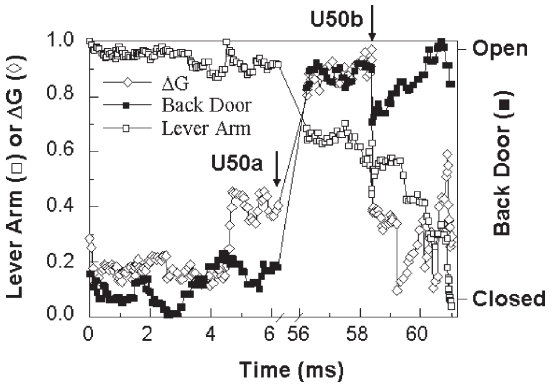


FIGURE 3: Free energy change in $\Delta G$ (◇), work producing lever arm displacement (□), and back door opening (■) for S1 during a representative M** → M transition. Quantities are rescaled to a unit maximum amplitude facilitating comparison of their shape relative to the time dimension demonstrating the synchronization of events at the active site and lever arm with changes in protein free energy. $\Delta G$ decreases during a spontaneous process, indicating the U50a transition presents a large energy barrier to the lever arm swing. Crossing the U50a barrier accompanies product release with the opening of the back door and unlocks the lever arm swinging motion to accomplish the power stroke. Simulation shows that coupling the U50a and U50b conformation transitions removes the free energy barrier to product release. The C-loop is a structured surface loop linking U50a and U50b whose structure is perturbed with actin binding. These circumstances suggest that perturbation of the C-loop with actin binding couples U50a and U50b transitions, causing product release and power stroke initiation.

change conformation in an all-or-nothing manner (one DOF per block domain). Inspection of S1 crystal structures (*3*, *4*, *44*) led to identification of block domains remaining structurally intact but moving relatively during hydrolysis (*4*, *43*, *44*). The partitioned S1, depicted in Figure 2, has block peptides designated N-terminal (amino acids 1−144, blue ribbon), U50a (amino acids 145−361, green ribbon), U50b (amino acids 362−462, red tube, top), loop 2 containing (amino acids 526−695, yellow ribbon), converter (amino acids 721−772, red ribbon, bottom), and lever arm (amino acids 773−812, white ribbon). Gear peptides are amino acids 463−525 and 696−720 (black stick backbone bonds). The C-loop and myopathy loop are labeled. Block domains move rigidly in a conformational trajectory until the transition when the domain transits instantaneously from the initial to final state. Alternatively, gear peptides make one-residue transitions in one DOF. Previously, we designated the U50a and U50b peptides as U50k and L50k, respectively (*29*), but have adopted here a new nomenclature to align it with the more conventional terminology. Conventional terminology has the upper 50 kDa domain containing both U50a and U50b while the lower 50 kDa domain contains the gear peptide of amino acids 463−525 and a portion of the loop 2-containing peptide.

MCMD simulation involves a free energy criterion for trial structure acceptance and rejection. The Gibbs free energy potential change ($\Delta G$) combines enthalpic ($\Delta H$) and constant temperature (kelvin) times entropic change ($T\Delta S$) in the relationship $\Delta G = \Delta H - T\Delta S$. We compute the free energy from the separate $\Delta H$ and $T\Delta S$ components and assign the changes in these quantities to regions in myosin (*29*). The 20 trajectories simulated for native S1 were mined for information characterizing the energy transduction mechanism. The active site Arg245−Glu468 salt bridge back door opens for phosphate release. Figure 3 shows the time dependence for the free energy change or $\Delta G$ (◇), the work producing lever arm displacement (□), and back door opening (■) for S1 during a representative M** → M transition. Quantities are normalized to a unit maximum amplitude to facilitate comparison of their shapes in time.

The U50a transition occurs at the vertical arrow to lower both enthalpy and entropy, but entropy dominates to increase free energy. The barrier delays simulation progress for ~50 ms. The entropy decreasing transition opens the back door and initiates lever arm movement. All conformation trajectories confirm that during ATPase the entropy-dominated U50a transition is a free energy barrier ensuring that product release is rate-limiting and prior to the lever arm swing in agreement with the conventional myosin mechanism. Compensating the U50a free energy-increasing (entropy-decreasing) barrier is the U50b free energy-decreasing (entropy-increasing) antibarrier (U50b transition occurs at ~59 ms in Figure 3).

A constrained S1 trajectory requiring simultaneous U50a−U50b transition removed the free energy barrier to product release, suggesting a mechanism for ATPase actin activation. U50b is part of the known actin binding site containing both the C-loop and the myopathy loop. The C-loop forms the U50a−U50b junction and is ideally located to initiate U50a−U50b coupling. We propose that the C-loop is the sensor that when perturbed by actin binding commits myosin to ATP turnover by instigating the simultaneous U50a−U50b conformation transition to release hydrolysis products.

## RESULTS

*Myosin and Actin-Activated Myosin ATPase*. We tested how mutations affect the mechanism of ATP hydrolysis in the expressed myosin by measuring enzymatic activities without actin. $K^+$EDTA- and $Ca^{2+}$ATPases without actin measured at a high ionic strength (nonphysiological ATPases) are sensitive indicators of perturbation of myosin from the native state. $K^+$EDTA-, $Ca^{2+}$-, and $Mg^{2+}$ATPases at saturating substrate

Table 2: Characterization of WT and Mutant HMM

| | ATPase ($s^{-1}$)[a,b] | | | actin-activated ATPase[b] | | | Scheme 1 $(K_{A1}K_{A2})^{-1}$ (nM)[d] | |
|---|---|---|---|---|---|---|---|---|
| | $K^+$EDTA | $Ca^{2+}$ | $Mg^{2+}$ ($\times 10^2$) | $V_{max}$ ($s^{-1}$) | $K_{ATPase}$ ($\mu$M) | motility[c] ($\mu$m/s) | apo | ADP |
| WT | 14.0 ± 0.9 | 5.9 ± 0.3 | 2.1 ± 0.6 | 0.72 ± 0.06 | 37 ± 11 | 0.25 ± 0.08 | 9 ± 1 | 25 ± 3 |
| G362A | 8.0 ± 1.0 | 6.6 ± 0.3 | 1.7 ± 0.2 | 0.87 ± 0.08 | 24 ± 6 | 0.48 ± 0.07 | 24 ± 2 | 26 ± 3 |
| G409V | 9.5 ± 0.4 | 4.2 ± 0.2 | 1.7 ± 0.2 | 0.76 ± 0.11 | 115 ± 29 | 0.29 ± 0.06 | 33 ± 5 | 47 ± 1 |
| cCl | 10.0 ± 1.6 | 2.4 ± 0.2 | 2.5 ± 0.1 | 0.23 ± 0.05 | 81 ± 38 | 0.1 ± 0.05 | 38 ± 2 | 54 ± 2 |
| sCl | 15.8 ± 0.4 | 4.0 ± 0.2 | 1.6 ± 0.2 | 0.12 ± 0.02 | 57 ± 31 | 0.1 ± 0.05 | 28 ± 3 | 46 ± 5 |

[a] The $K^+$EDTA-ATPase assay was conducted on samples at 37 °C in 250 $\mu$L aliquots containing 0.15−0.30 $\mu$M expressed HMM, 0.6 M KCl, 10 mM EDTA, 25 mM Tris-HCl (pH 8.0), and 2 mM ATP. The $Ca^{2+}$ATPase assay was identical to the $K^+$EDTA-ATPase assay except 10 mM $CaCl_2$ replaced the EDTA. [b] The $Mg^{2+}$ATPase assay was conducted on samples at 25 °C in 300 $\mu$L aliquots containing 0.23 $\mu$M expressed HMM, 30 mM KCl, 2 mM $MgCl_2$, 0.2 mM $CaCl_2$, 0.5 mM DTT, 30 mM Tris (pH 7.6), and 1 mM ATP. HMM was phosphorylated by adding 40 $\mu$g/mL recombinant MLCK and 10 $\mu$g/mL bovine brain calmodulin to the assay. EGTA was added to stop the reaction. The actin concentration varied from 0 to 140 $\mu$M. [c] Conditions described in Experimental Procedures. [d] The strong binding assay was performed at 20 °C in 25 mM Tris (pH 7.5), 0.1 M KCl, 2 mM $MgCl_2$, 1 mM DTT, and 1 $\mu$g/mL leupeptin.

concentrations are listed in Table 2 for WT and mutant proteins. $K^+$EDTA-ATPases are modestly suppressed in the mutants compared to control except for sCl where the level is slightly higher. $Ca^{2+}$ATPases are likewise modestly perturbed in the mutants. The physiological $Mg^{2+}$ATPases are statistically unchanged in the mutants compared to WT. These data suggest the active sites of all proteins are functionally intact. Differences between mutant and WT proteins emerge with introduction of actin.

Actin-activated myosin ATPase of G362A has a $V_{max}$ just significantly higher than that of WT while $K_{ATPase}$ is unaffected. We previously reported a somewhat higher $K_{ATPase}$ and unchanged $V_{max}$ compared to those of WT (*38*), but recent comparisons among a wider set of expressed constructs convinced us to revise the estimates. In the C-loop chimeras, actin-activated ATPase inhibition is indicated mainly by a lower $V_{max}$. Unlike the C-loop, the myopathy loop contains an unusual clustering of mutations implicated in heart disease, including the G409V substitution (*45*). The clinical phenotype for G409V is asymmetric septal hypertrophy, but no structural studies of affected tissues have been reported to the best of our knowledge. G409 is a highly conserved residue in the U50b domain also containing the C-loop. Table 2 summarizes characterization of this mutation in the HMM model protein. G409V contrasts with the C-loop mutations by affecting principally $K_{ATPase}$ rather than $V_{max}$.

*Strong Actin Binding Assay*. The actomyosin dissociation constants defined in Scheme 1, $1/(K_{A1}K_{A2})$, for WT and mutants are listed in Table 2. All constructs exhibit reduced actin affinity compared to that of WT as expected for mutations in the actin binding site (either C-loop or myopathy loop). The binding of ADP weakened the actin binding affinity for all the HMMs except G362A which does not have reduced actin affinity in the presence of MgADP within error limits.

*Kinetics of Nucleotide Binding and Dissociation for WT, G409V, and G362A*. We studied nucleotide binding to and dissociation from HMM by using rapid kinetic stopped-flow measurements. Schemes 3 and 4 involve the events to be characterized with myosin (M), actin (A), ATP (T), ADP (D), and phosphate (P). Step numbering is consistent with the actomyosin cycle in Scheme 5 in the Supporting Information. Rates are denoted with a lowercase *k* and equilibrium constants with an uppercase *K*.

*(i) Myosin Kinetics in the Absence of Actin*. The binding of ATP to HMM was detected using the nucleotide sensitive

Scheme 3

$$M + T \underset{k_{-1}}{\overset{k_1}{\leftrightarrow}} MT \underset{k_{-2}}{\overset{k_2}{\leftrightarrow}} M^*T \underset{k_{-3}}{\overset{k_3}{\leftrightarrow}} M^{**}DP \underset{k_{-4}}{\overset{k_4}{\leftrightarrow}} M^{\wedge}DP \underset{k_{-5}}{\overset{k_5}{\leftrightarrow}} M^{\wedge}D \underset{k_{-6}}{\overset{k_6}{\leftrightarrow}} MD \underset{k_{-7}}{\overset{k_7}{\leftrightarrow}} M$$

Scheme 4

$$\begin{bmatrix} AM + T \overset{K_1}{\leftrightarrow} A \cdot M \cdot T \overset{k_2}{\rightarrow} A - M \cdot T \rightarrow A + MT \\ + D \updownarrow K_{AD} \\ A \cdot M \cdot D \end{bmatrix}$$

W510 fluorescence (*46*). When 0.25 $\mu$M WT HMM was mixed with 100 $\mu$M ATP, the fluorescence intensity increased by 10%. The exponential fit to the fluorescence transient gave a $k_{obs}$ of 28.5 $s^{-1}$. The experiment was repeated at various ATP concentrations (between 10 and 500 $\mu$M). The transients were fitted with a single-exponential function and the rates ($k_{obs}$) plotted as a function of ATP concentration (Figure 4A). At low ATP concentrations, the second-order binding constant ($K_1k_2$) was estimated from a linear fit to be $(0.44 \pm 0.01) \times 10^6$ $M^{-1}$ $s^{-1}$. At higher ATP concentrations, the curve was quasi-hyperbolic in ATP concentration, such that $k_{obs} = (k_3 + k_{-3})[ATP]/([ATP] + 1/K_1)$. A hyperbola fit to the plot gave a half-saturation ATP concentration of 50 ± 13 $\mu$M ($1/K_1$ in Scheme 3) and a maximal $k_{obs}$ value of 37 ± 3 $s^{-1}$ ($k_3 + k_{-3}$ in Scheme 3).

To measure the rate of binding of ADP to WT HMM, we repeated the binding assay with ADP. WT HMM (0.25 $\mu$M) was mixed with ADP at various concentrations. The tryptophan fluorescence intensity increased by 4−6% upon ADP binding. The $k_{obs}$ values were obtained from single-exponential fits and showed a hyperbolic tendency in ADP concentration. The maximal $k_{obs}$ value was 11 ± 1 $s^{-1}$ ($k_{-6}$ in Scheme 3), and the half-saturation ADP concentration was 8.6 ± 1.6 $\mu$M ($K_7$ in Scheme 3).

The difference between the tryptophan fluorescence changes observed upon ATP (10%) and ADP (4−6%) binding allowed us to measure the rate of dissociation of ADP from WT HMM. WT HMM (0.5 $\mu$M) was pre-equilibrated with ADP (20 $\mu$M) (these concentrations are given as they were established before the stopped-flow mixing). Then the solution of ADP and WT HMM was mixed with 100 $\mu$M ATP (concentration after the mix) in the stopped-flow system. As the ATP was in large excess, after the

Table 3: Rate and Equilibrium Constants for the Interaction of HMM with Nucleotides

| | Scheme 3 constant | WT | G409V | G362A |
|---|---|---|---|---|
| ATP (Trp) | $K_1k_2$ ($\times 10^6$ $s^{-1}$ $M^{-1}$) | 0.44 ± 0.01 | 0.52 ± 0.01 | 0.20 ± 0.01 |
| | $1/K_1$ ($\mu$M) | 50 ± 13 | 45 ± 12 | 166 ± 67 |
| | $k_{-3} + k_3$ ($s^{-1}$) | 37 ± 3 | 48 ± 4 | 54 ± 9 |
| mATP | $K_1k_2$ ($\times 10^6$ $s^{-1}$ $M^{-1}$) | 1.3 ± 0.1 | nd[a] | nd[a] |
| ADP (Trp) | $k_{-6}$ ($s^{-1}$) | 11 ± 1 | nd[a] | nd[a] |
| | $K_7$ ($\mu$M) | 8.6 ± 1.6 | nd[a] | nd[a] |
| | $k_6$ ($s^{-1}$) | 2.7 ± 0.1 | 2.3 ± 0.1 | 22 ± 0.1 |
| mADP | $k_{-6}/K_7$ ($\times 10^6$ $s^{-1}$ $M^{-1}$) | 1.1 ± 0.1 | nd[a] | nd[a] |
| | $k_6$ ($s^{-1}$) | 1.0 ± 0.1 | 0.8 ± 0.1 | nd[a] |

| | Scheme 4 constant | WT | G409V | G362A |
|---|---|---|---|---|
| ATP-induced actin dissociation | $1/K_1$ ($\mu$M) | 125 ± 17 | 122 ± 25 | nd[a] |
| | $k_2$ ($s^{-1}$) | 57 ± 2 | 60 ± 3 | nd[a] |
| | $K_1k_2$ ($\times 10^6$ $s^{-1}$ $M^{-1}$) | 0.46 | 0.49 | nd[a] |
| with ADP | $K_{AD}$ ($\mu$M) | 84 ± 4 | 69 ± 7 | 39 ± 3 |

[a] Not determined.

dissociation of ADP the ATP replaced the ADP in the nucleotide binding pocket of HMM and the fluorescence changes were observed. The amplitude of the fluorescence transient was 2−3% (Figure 4B). The single-exponential fit to the time dependence of the tryptophan fluorescence gave a $k_{obs}$ value of 2.6 $s^{-1}$. When experiments were repeated by using a 4-fold higher ATP concentration (400 $\mu$M), the $k_{obs}$ was practically unchanged (2.7 $s^{-1}$). The ATP concentration independence of $k_{obs}$ indicates that the first-order rate of ADP dissociation is rate-limiting for tryptophan fluorescence changes and the value of $k_{obs}$ reflects the rate of dissociation of ADP from WT HMM ($k_6$ in Scheme 3).

Nucleotide binding and myosin isomerization were also characterized with the fluorescent nucleotides mant-ATP (mATP) and mant-ADP (mADP) (*47*). When WT HMM (0.25 $\mu$M) was mixed with mATP (10 $\mu$M), the fluorescence intensity increased by 3−4%. The transient was analyzed by fitting a single-exponential function and gave a $k_{obs}$ value of 9.9 $s^{-1}$. The experiment was repeated at various mATP concentrations between 5 and 20 $\mu$M. Note that higher mATP concentrations were not suitable for these experiments because of the increase in the background provided by the unbound mATP. The $k_{obs}$ value increased linearly in mATP concentration. The second-order rate constant for binding of mATP to WT HMM was estimated from the slope of the mATP concentration dependence of the $k_{obs}$ to be $(1.3 \pm 0.1) \times 10^6$ $M^{-1}$ $s^{-1}$. Similar experiments with mADP gave a second-order rate constant ($k_{-6}/K_7$) of $(1.1 \pm 0.1) \times 10^6$ $M^{-1}$ $s^{-1}$. The rate of dissociation of mADP from HMM was estimated to be 1 $s^{-1}$ by experiments paralleling those for measuring ADP dissociation.

The experiments with mant nucleotides gave kinetic results somewhat different from those obtained with ATP or ADP (Table 3). Similar deviations of the mant versus native nucleotides were observed previously with other myosin isoforms (e.g., ref (*48*)), indicating that the attachment of the mant group can modify the kinetic properties of the nucleotides.

Most experiments were repeated with G409V and G362A to obtain parameters summarized in Table 3.

*(ii) Myosin Kinetics in the Presence of Actin*. The kinetics of the interaction between the nucleotides and actomyosin (AM) were investigated by using p-F-actin. Rapid mixing in the stopped-flow system of the acto-HMM complex with excess ATP results in a time-dependent pyrene fluorescence increase reflecting AM dissociation (Scheme 4). In these measurements, p-F-actin (100 nM) was equilibrated with WT HMM (100 nM) and then mixed with excess ATP in the stopped-flow system. When 200 $\mu$M ATP was applied, the pyrene fluorescence increased by 17%. An exponential fit to the pyrene transient gave a $k_{obs}$ value of 35.7 $s^{-1}$. The experiment was repeated at various ATP concentrations between 10 $\mu$M and 2.5 mM. The obtained $k_{obs}$ values were plotted as a function of ATP concentration, and the curve was hyperbolic. The hyperbola fit to the plot gave a half-saturation ATP concentration of 125 ± 17 $\mu$M ($1/K_1$ in Scheme 4) and a maximal rate of 57 ± 2 $s^{-1}$ ($k_2$ in Scheme 4). The ratio of these parameters estimates the second-order rate constant to be 0.46 × $10^6$ $M^{-1}$ $s^{-1}$ ($K_1k_2$ in Scheme 4). These experiments were also conducted with the G409V mutant with results similar to those observed for WT HMM (Table 3).

To estimate the affinity of ADP for the actomyosin complex, actomyosin dissociation by ATP experiments were repeated in the presence of varying ADP concentrations. p-F-Actin (0.25 $\mu$M) was equilibrated with 0.25 $\mu$M WT HMM and then mixed with ATP (100 $\mu$M) and ADP (varied) in the stopped-flow system. In these experiments, the ATP and ADP are competing for the binding site in HMM. The pyrene fluorescence changes reflect the ATP-induced dissociation of the HMM from actin. Provided that the equilibrium between the nucleotides and the actomyosin is always established rapidly, the ADP concentration dependence of the observed rates reflects the affinity of ADP for the actomyosin. The single-exponential rate for pyrene fluorescence change ($k_{obs}$) decreased as $(1 + [ADP]/K_{AD})^{-1}$ for an increasing ADP concentration, where $K_{AD}$ is the apparent equilibrium dissociation constant for binding of ADP to the actomyosin complex (see Scheme 4). The $k_{obs}$ values were plotted as the function of ADP concentration (Figure 4C). The experiments were conducted for WT, G409V, and G362A, giving $K_{AD}$ values of 84, 69, and 39 $\mu$M, respectively (Table 3). According to these results, ADP binding to AM ($K_{AD}$) was the tightest for the G362A mutant.

The kinetic data collected suggest that the G409V replacement minimally affects the active site kinetics. In contrast, G362A has altered active site properties, including weaker association with ATP ($K_1$) and the larger dissociation rate of ADP from the binding site ($k_6$), demonstrating an active site−C-loop link.

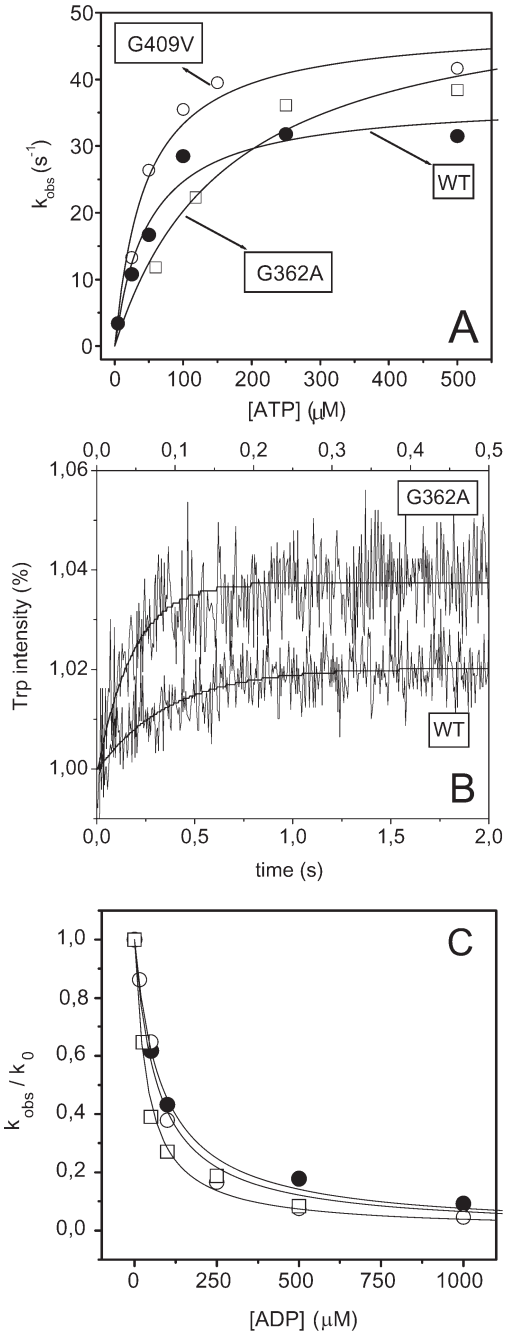


FIGURE 4: (A) ATP concentration dependence of $k_{obs}$ measured for WT (●), G409V (○), and G362A (□). ATP binding to HMM in the absence of actin was assessed using tryptophan fluorescence changes. WT HMM was mixed with ATP, and the changes in the tryptophan fluorescence were recorded and fitted with single exponential giving $k_{obs}$. The hyperbola fits to the plots in the form $k_{obs} = (k_{-3} + k_3)[ATP]/([ATP] + 1/K_1)$ are solid lines giving $k_{-3} + k_3$ and $K_1$ values quoted in Table 3.

(B) Dissociation of ADP from HMM in the absence of actin as measured by tryptophan fluorescence changes in time. HMM was pre-equilibrated with ADP and then mixed with ATP in the stopped-flow system. The exponential fit to the transients gave $k_{obs}$. Note that the shorter time scale at the top of the plot corresponds to the G362A data. Experiments with G409V closely resembled those with WT. The $k_{obs}$ values in these experiments corresponded to rate $k_6$ in Scheme 3.

(C) ADP concentration dependence of $k_{obs}$ measured for WT (●), G409V (○), and G362A (□) bound to p-F-actin. p-F-actin was equilibrated with WT HMM and then mixed with ATP (100 μM) and ADP (various concentrations) in the stopped-flow system. The exponential fit to the pyrene fluorescence changes transients gave $k_{obs}$ rates for ATP-induced dissociation of the HMM from actin (Scheme 4). The ADP concentration dependence of $k_{obs}$ reflects the affinity of ADP for the actomyosin, giving $K_{AD}$ (Table 3). $k_0$ is $k_{obs}$ at 0 mM ADP.

Assuming that the ADP association rates are similar for the three investigated forms of HMM, the faster dissociation of ADP from G362V HMM suggests a weaker ADP affinity in the absence of actin. On the other hand, the affinity of ADP for the actomyosin complex appeared to be tighter for the G362A HMM mutant than for WT or G409V. These observations suggest that the weakening effect of actin on the ADP affinity was smaller for G362V than for WT or G409V.

Kinetic parameters obtained in this study differ somewhat from those reported previously due mainly to the choices of ionic strength. Kinetic parameters summarized in Table 3 were observed in 100 mM KCl. The second-order constant for ATP binding to WT HMM ($K_1k_2 = 0.44 \times 10^6$ $M^{-1}$ $s^{-1}$ in Table 3) is faster than that observed by Onishi et al. (*49*) in 450 mM KCl, where $K_1k_2 = 0.25 \times 10^6$ $M^{-1}$ $s^{-1}$, and slower than that reported by Rosenfeld et al. (*50*) in 20 mM KCl, where $K_1k_2 = 1.2 \times 10^6$ $M^{-1}$ $s^{-1}$. Similarly, mATP binding was also slower in 450 mM KCl (*49*) than in our work. The equilibrium binding constant for ATP ($K_1$) and $k_3 + k_{-3}$ rates are larger at 450 mM KCl (compare 50 μM and 37 $s^{-1}$ in Table 3 to 650 μM and 166 $s^{-1}$, respectively) (*49*). The ADP dissociation rate of 3 $s^{-1}$ at 100 mM KCl (*51*) agrees favorably with the value determined here [2.7 $s^{-1}$ (Table 3)]. The second-order rate constant for ATP-induced dissociation of the acto-HMM complex was $0.3 \times 10^6$ $M^{-1}$ $s^{-1}$ at 100 mM KCl (*51*) which compares favorably to our value of $0.46 \times 10^6$ $M^{-1}$ $s^{-1}$ (Table 3) and is less than the value of $0.83 \times 10^6$ $M^{-1}$ $s^{-1}$ measured at 20 mM KCl (*50*).

Kinetic simulation of the actomyosin cycle with rate constants taken from Tables 2 and 3 and from the literature is discussed in the Supporting Information. The actomyosin ATPase cycle is used to compute the myosin $Mg^{2+}$ATPase rate, $V_0$, the actin-activated ATPase versus actin concentration giving $V_{max}$ and $K_{ATPase}$, and duty ratio $r_d$ estimated from the kinetics by the fraction of strongly actin bound myosin at a saturating actin concentration. The duty ratio is the fraction of time that a motor can produce work; hence, it is a critical determinant of muscle function. Chemical kinetics and motility velocity are measured on different myosin-based assays, but they are dependent through eq 1

$$v_{motil} = \frac{d V_{max}}{r_d} \quad (1)$$

where $d$ is the myosin step size (assumed to be 0.01 μm) and $v_{motil}$ is the actin sliding velocity measured by the in vitro assay. The whole cycle simulation confirms that both mutants have (i) phosphate release that is rate-limiting in the presence or absence of actin and (ii) a duty ratio of ~0.05 (*52*).

*In Vitro Motility of G362A and G409V*. Table 2 lists average motility velocities for WT, G362A, and G409V. The average motility velocities for the C-loop chimeras are also listed for the sake of comparison. In vitro motility experiments in Table 2 were conducted at a high HMM surface density where motility velocity is maximal. We made a more detailed analysis of the effect of C-loop chimeras on in vitro velocity that is described in the next section.

In vitro motility velocity sharply contrasts in the various mutants tested. The velocity of G362A is significantly higher than those of WT and other mutants as reported previously (*38*). G409V and WT are not significantly different. Motility velocity in the C-loop chimeras is attenuated compared to that of WT, again suggesting a role for the native C-loop in mediating actomyosin interaction.

Table 4: In Vitro Motility Histogram Global Analysis

| group[a] | myosin/actin | surface density[b] | population distribution (%)[c] slow | fast | ⟨v⟩ (μm/s)[d] |
|---|---|---|---|---|---|
| 1 | WT/A | low | 43 | 57 | 0.15 |
| | WT/A | high | 19 | 81 | 0.18 |
| | WT/HCTm-A | low | 25 | 75 | 0.17 |
| | WT/HCTm-A | high | 9 | 91 | 0.19 |
| | cCl/A | low | 84 | 16 | 0.10 |
| | cCl/A | high | 90 | 10 | 0.09 |
| | sCl/A | low | 96 | 4 | 0.10 |
| | sCl/A | high | 99 | 1 | 0.09 |
| | sCl/HCTm-A | low | 99 | 1 | 0.09 |
| | sCl/HCTm-A | high | 99 | 1 | 0.09 |
| | cCl/SKTm-A | low | 96 | 4 | 0.09 |
| 2 | WT/SKTm-A | low | 49 | 51 | 0.13 |
| 3 | WT/SKTm-A | high | 58 | 42 | 0.11 |
| 2 | cCl/HCTm-A | high | 92 | 8 | 0.10 |

[a] Group 1 histograms: $v_1 = 0.103\ \mu$m/s, $v_2 = 0.204\ \mu$m/s, $w_1 = 0.048\ \mu$m/s, and $w_2 = 0.082\ \mu$m/s. Group 2 histograms: $v_1 = 0.115\ \mu$m/s, $v_2 = 0.166\ \mu$m/s, $w_1 = 0.054\ \mu$m/s, and $w_2 = 0.076\ \mu$m/s. Group 3 histograms: $v_1 = 0.085\ \mu$m/s, $v_2 = 0.152\ \mu$m/s, $w_1 = 0.048\ \mu$m/s, and $w_2 = 0.092\ \mu$m/s. Peak velocity and width errors are ±0.002. [b] The myosin surface density was varied using 0.15 or 0.35 mg/mL anti-myc antibody flow-through. [c] Population of Gaussian-distributed filament velocities with peak velocity $v_1$ and width $w_1$ (slow) or $v_2$ and $w_2$ (fast) given by $100a_1$ or $100a_2 = 100 \times (1 - a_1)$. Errors are ±5. [d] The average velocity $[\langle v\rangle \geq a_1v_1 + (1 - a_1)v_2]$ has an error of ~20%.

MCMD simulation of S1 in the M** → M trajectory suggests the involvement of the C-loop at the U50a−U50b junction in initiating U50a−U50b coupling. We proposed that the C-loop is the sensor that when perturbed by actin binding commits myosin to ATP turn over by instigating the simultaneous U50a−U50b conformation transition to release hydrolysis products. According to MCMD simulation, the C-loop should regulate the rate-limiting step in the actomyosin cycle. Kinetics described in the previous section showed that phosphate release is the rate-limiting step for G362A. Data in Table 2 show the G362A in vitro motility velocity is enhanced compared to that of WT. Thus, the G362A substitution must increase the rate of the rate-limiting step in the myosin cycle to enhance motility velocity, demonstrating the involvement of the C-loop in phosphate release.

*In Vitro Motility of C-Loop Chimeras.* WT velocity histograms were not well represented by a single Gaussian curve. They contained two apparent subpopulations of actin filament velocities modeled by the sum of two Gaussians where free parameters are peak velocities ($v_1$ and $v_2$), widths ($w_1$ and $w_2$), and one amplitude ($A_1$) multiplying one of the Gaussians. Amplitude $A_1$ represents the number of filaments moving with Gaussian-distributed velocities characterized by peak velocity $v_1$ and width $w_1$. Amplitude $A_2 = N - A_1$ for $N$, the total number of observations.

Data were examined for variability among individual measurements to assess variance ($\sigma^2$) for each point in the velocity histograms. $\chi^2$ was computed with eq 2

$$\chi^2 = \sum_i \frac{1}{\sigma_i^2}[y_i - y(x_i)]^2 \qquad (2)$$

where $y_i$ is the number of events in velocity increment $x_i - x_{i-1}$ and $y(x_i)$ is the fitted curve. For the reduced $\chi^2$, $\chi_\nu^2 = \chi^2/\nu$, where $\nu$ is the degree of freedom (*53*). Global data analysis of 14 conditions had peak velocities and widths common for all data sets and a Gaussian amplitude that varied for each histogram while minimizing $\chi^2$ (total free parameters are four nonlinear parameters $v_1$, $v_2$, $w_1$, and $w_2$ and 14 linear parameters corresponding to amplitude $A_1$ in 14 conditions). $\chi^2$ evaluates the choice of the parent distribution (sum of two Gaussians) and the noisiness of the data. The first objective is to evaluate the appropriateness of the parent distribution, and we did this with

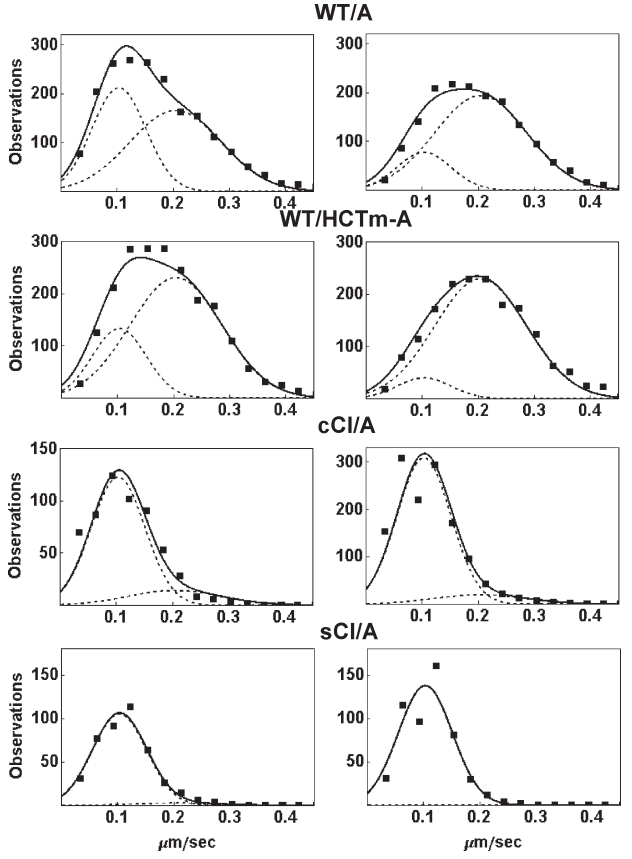


FIGURE 5: In vitro motility histograms (■) and their decomposition into group 1 Gaussian distributions (—) for WT, cCl, and sCl HMM. Rh-phalloidin-labeled bare actin (A) or that with bound human cardiac tropomyosin (HCTm-A) glides over the surface-bound HMM. The fitted black curves are the sums of dashed curves. The left (right) column corresponds to low (high) myosin surface densities.

the F-test (*53*). The F-test compares $\chi_\nu^2$ ratios from different models to evaluate their appropriateness, while the data noisiness effect tends to cancel. We compared the global fit to the individual histogram fit and found that only three histograms were inconsistent with the global model.

The second objective is to characterize motility in the systems tested. Table 4 summarizes the results. Eleven motility histograms (group 1) are consistent with one global parameter set. Two other parameter sets (groups 2 and 3) were needed to fit the remaining histograms. Figure 5 shows in vitro motility histograms and their decomposition into group 1 Gaussian distributions (dashed curves) for WT HMM, cCl, and sCl. The fitted black curves are the sum of two dashed curves. The global analysis permits direct comparison of fractional populations ($a_1 = A_1/N$, and $a_2 = 1 - a_1$) within a given group. It also reduces model degrees of freedom without significantly deteriorating the goodness of fit, thereby permitting a clearer overall interpretation of data.

Results in Table 4 show that C-loop replacement with sequences from different myosin isoforms diminishes actin motility. Furthermore, HCTm-actin, but not SKTm-actin, increases actin motility in WT. Detailed analysis of the motility results indicates that (i) a higher myosin surface density or HCTm-actin increases average velocity by promoting slow myosin to the fast myosin subpopulation (group 1, top four rows, compare fractional populations), (ii) SKTm-actin inhibits promotion of slow myosin to the fast myosin subpopulation (groups 2 and 3 with SKTm), and (iii) the motility mechanism involves the C-loop because its modification eliminates the fast myosin subpopulation even with HCTm-A (group 1, rows 5−11, compare fractional populations).

## DISCUSSION

The U50a and U50b myosin domains make up a large portion of the actin binding site and are linked by the C-loop actin binding peptide. They play an important role in the MCMD simulation of myosin trajectory during the M** → M conformation transition (*29*). U50a encompasses the free energy (mostly entropy-decreasing) barrier to phosphate release, inhibiting myosin ATPase in the absence of actin. The U50b containing both the C-loop and the myopathy loop encompasses the free energy (mostly entropy-increasing) antibarrier to product release in the absence of actin. The C-loop is the U50a−U50b junction and is ideally located to initiate U50a−U50b coupling. Simulation suggests C-loop perturbation synchronizes the U50a (barrier) conformation change with the U50b (antibarrier) conformation change to eliminate the overall free energy barrier to product release. We hypothesize that actin binding perturbs the C-loop to initiate the chain of events. An actin contact detector at the junction of matched entropy-decreasing and entropy-increasing peptides may represent a general design for a deactivatable free energy barrier where in this case the reaction is that of myosin ATPase and the catalyst is actin.

Substantial experimental evidence suggests that the C-loop binds actin and communicates bidirectionally with the active site. Bound ATP or trapped ADP·$V_i$ accelerates C-loop proteolysis in $\beta$S1, demonstrating the influence of the active site on C-loop structure (*17*). Tryptic cleavage of the C-loop in $\beta$S1 eliminated actin-activated myosin ATPase and lowered actomyosin affinity, demonstrating the influence of the C-loop on active site structure (*17*). When the peptide backbone serves as a line of communication between distant sites, intervening highly conserved glycines are logical targets for Gly-to-Ala mutagenesis. The highly conserved G362 residue fits the profile, suggesting the G362A substitution might perturb active site−C-loop communication. The tip of the C-loop at R371 (Table 1) is the trypsin sensitive point in $\beta$S1 within a cluster of charged residues potentially serving as an electrostatic actin binding site. The replacement of the positively charged R371 with a negatively charged glutamic acid (smR370E because smooth muscle myosin has R370) might disturb an electrostatic interaction with actin.

ATPases in G362A and smR370E are little changed compared to WT, but the differences between mutant and WT proteins are amplified by introduction of actin. Actin-activated myosin ATPase of smR370E has a higher $K_{ATPase}$, indicating a weaker affinity for actin in the presence of ATP and a 2-fold higher $V_{max}$ compared to that of WT (*38*). The latter indicates the substitution affects actin regulation of ATPase. With G362A, we report here that $V_{max}$ is just significantly higher than that of WT while $K_{ATPase}$ is unaffected. We now conclude that both smR370E and G362A substitutions affect $V_{max}$. Changes in $V_{max}$ suggest the C-loop is an actin contact sensor communicating initiation of the actin binding event to the active site and triggering ATPase activation. Lately, other mutants in the C-loop of a truncated (without light chains) mutant Dc myosin II motor domain (i.e., a C-loop mutant of a mutant protein from which tryptophans were removed except W510) have confirmed perturbation of actin binding, but their effect on $V_{max}$ was inconclusive (*28*).

Kinetics experiments summarized in Table 3 indicate that other active site kinetics are substantially affected by the G362A substitution while a myopathy loop substitution, G409V, has little effect on the active site kinetics. Notably, the rate of dissociation of ADP from G362A is enhanced ~10-fold compared to those of WT and G409V. Simulation of the actomyosin cycle of G362A shows that as in WT the phosphate release step is rate-limiting. The enhanced in vitro motility velocity of G362A compared to that of WT demonstrates the involvement of the C-loop in the phosphate release step.

The clinical phenotype for G409V is asymmetric septal hypertrophy, but no structural studies of affected tissues have been reported (*45*). In vitro experiments (Table 2) showed no change in motility velocity, a higher $K_{ATPase}$ from the actin-activated myosin ATPase, and a higher $K_{A1}K_{A2}$ (Scheme 1) from strong actin binding measurements, for G409V compared to WT. Actomyosin cycle simulation (Supporting Information) shows that the duty ratio is unchanged from that of WT by the G409V substitution. The significantly higher $K_{ATPase}$ and $K_{A1}K_{A2}$ binding constants for G409V compared to those of WT indicates weaker actin affinity in both weakly and strongly actin binding states. This alteration alone is unlikely to cause the clinical phenotype because a high actin concentration in the cardiac muscle tissue probably mitigates the modestly lower myosin affinity for actin. Lower affinity to actin may indicate a generally degraded fit between myosin and actin. Previous results on the smooth muscle model R405W/Q mutants exhibited corrupted ordering of cross-bridge orientation when strongly bound to F-actin (*54*). Cross-bridge orientation of strongly actin bound G409V is currently under investigation.

We extended the experimental work to smooth muscle HMM C-loop chimeras in which skeletal (sCl) and cardiac (cCl) myosin C-loops were substituted for the native sequence. In both C-loop chimeras, actin-activated ATPase inhibition is indicated mainly by the substantially lower $V_{max}$, with the sCl chimera having the

stronger suppression of $V_{max}$ (Table 2). Results in Table 4 and Figure 5 show how the myosin chimeras modify actin in vitro motility. We evaluated the sliding velocity of unregulated actin and Tm-actin for the cardiac or skeletal Tm isoforms (SKTm and HCTm, respectively). Motility data were collected as a function of myosin surface density, with unregulated actin, SKTm-actin, and HCTm-actin for WT, cCl, and sCl. The large body of data collected was fitted in a global analysis enabling us to identify and characterize two velocity subpopulations in the species tested. Statistical tests permitted objective evaluation of the parent distribution suitability and the best fitting global parameters. Results indicate that for WT myosin, increased myosin surface density and HCTm-actin are additive in promoting slow to fast subpopulation conversion while SKTm-actin does not promote conversion and nullifies the effect of increasing myosin surface density on conversion. Modification of the smooth muscle C-loop into either skeletal or cardiac isoforms eliminates the fast myosin subpopulation even with HCTm-A.

The results indicate that severe geometrical constraints on actomyosin at a low myosin surface density are relaxed by increasing myosin surface density when the probability for one or more most favorable (for velocity) actomyosin interactions increases. Similarly, HCTm-actin promotes the most favorable actomyosin interactions by lowering the inhibiting geometrical constraint barriers with an effect on actin. In contrast, SKTm-actin raises the inhibiting geometrical constraint barriers to the level where surface density is unable to promote the most favorable actomyosin interactions. In previous studies, SKTm and HCTm isoforms were suggested to bind differently on an unregulated actin filament, with HCTm increasing actin motility velocity but SKTm having no effect (*41*). Other work showed the cardiac and skeletal Tm isoforms maintaining different coordinations with actin (*55*).

Data from sCl and cCl suggest the element initiating maximal myosin activation by actin resides in the C-loop. The C-loop has been shown to interact with Tm in Tm-actin, supporting the notion that the C-loop, and possibly its interaction with Tm, is intimately involved in actin activation of myosin (*27*). HCTm-actin is more tolerant of unfavorable actomyosin geometry relative to bare actin because it can promote myosin to the fast population at a lower myosin surface density. We suggest this is due to more permissive C-loop−actin contact via HCTm mediation. Geometrical constraints in the motility assay, absent from the in-solution assay of myosin actin activation, amplify the significance of the C-loop−actin and C-loop−Tm-actin interaction. The limited myosin ATPase actin activation in the C-loop chimeras suggests that the actin interaction triggering the allosteric effect on the active site originates from an isoform specific interaction of the C-loop with actin.

C-loop−active site allostery in triggering actin activation of ATPase and motility is likely conserved in the myosin family because the structured surface loop is a conserved feature in all myosin motor domains that have crystal structures. Nonetheless, detailed interactions between the C-loop in various myosin isoforms and actin probably differ since the C-loop sequence is not fully conserved, and our data show it is an isoform specific interaction. Our work suggests that the C-loop instigates the coordinated structural transition in adjacent conserved myosin domains in response to actin binding. The C-loop appears to function in this role with modest sequence variability, albeit suboptimally, because cCl and sCl smooth muscle myosin chimeras are suboptimally actin-activated and motile. Sequence specific optimal actin activation and motility could reflect coevolution of the actomyosin coordination and the C-loop contact sensor. If so, the C-loop and actomyosin interface sites should mutually constrain evolution at the two sites (C-loop is a part of the actin binding site, but most of the actomyosin interface is spread over a large surface area of the myosin), causing conservation of critical residues in both sites as observed in other proteins and other allosteric pathways in myosin (*56*−*58*).

## CONCLUSION

We hypothesized that the C-loop is an actin contact sensor initiating actin activation of the myosin ATPase and have provided computational and experimental evidence supporting this role for the C-loop in the mechanism. MCMD simulation of the power stroke indicated that the U50a and U50b domains encompass the free energy barrier to product release and a potential antibarrier, respectively. Simulation shows that coupling the U50a and U50b conformation transitions removes the free energy barrier to product release. The C-loop is a structured surface loop linking U50a and U50b whose structure would be perturbed with actin binding. These circumstances suggest that perturbation of the C-loop with actin binding couples U50a and U50b transitions causing product release and power stroke initiation.

Experimental evidence suggests that C-loop binds actin and communicates bidirectionally with the active site. Bound ATP or trapped ADP·$V_i$ accelerates C-loop proteolysis in $\beta$S1, demonstrating the influence of the active site on C-loop structure (*17*). Tryptic cleavage of the C-loop in $\beta$S1 eliminated actin-activated myosin ATPase and lowered actomyosin affinity, demonstrating the influence of the C-loop on active site structure and affinity for actin (*17*). Site-directed mutagenesis targeted two residues within the C-loop. Kinetic and in vitro experiments on WT and mutant smooth muscle myosin showed the mutants reduced actin affinity and specifically affected $V_{max}$ in actin-activated ATPase, again demonstrating the ability of the C-loop to affect the active site.

Smooth muscle HMM C-loop chimeras were constructed having skeletal (sCl) and cardiac (cCl) myosin C-loops substituted for the native sequence. In both cases, actin-activated ATPase inhibition is indicated mainly by the substantially lower $V_{max}$. In vitro motility was also sharply inhibited in the chimers. Motility data were collected as a function of myosin surface density, with unregulated actin, and with skeletal and cardiac isoforms of tropomyosin-bound actin for WT, cCl, and sCl. Slow and fast subpopulations of myosin velocities in the WT species representing geometrically unfavorable and favorable actomyosin interactions, respectively, were discovered. Unfavorable interactions are possible at all the surface densities tested. Favorable interactions are more probable at higher myosin surface densities. Cardiac Tm-actin promotes the favorable actomyosin interactions by lowering the inhibiting geometrical constraint barriers with a structural effect on actin. Neither higher surface density nor cardiac Tm-actin can accelerate motility velocity in cCl or sCl, suggesting the element initiating maximal myosin activation by actin resides in the C-loop.

## ACKNOWLEDGMENT

We thank Hirofumi Onishi from the Japan Science and Technology Agency for cDNA of a recombinant WT chicken gizzard smooth muscle HMM and Danuta Szczesna-Cordary

from the University of Miami for the tropomyosins. We also thank Richard D. Bennett, Andrew Hipp, Jinhui Li, Ryan Raver, and Emanuel E. Strehler (Mayo Clinic College of Medicine, Mayo Clinic, Rochester, MN), Edina Meleg (University of Pécs), and Susanna Garamszegi (University of Miami) for their expert assistance in various aspects of the project.

## SUPPORTING INFORMATION AVAILABLE

Actomyosin kinetic simulation indicates the duty ratio and other systemic parameters in WT and mutant smooth muscle HMM. This material is available free of charge via the Internet at http://pubs.acs.org.

## REFERENCES

1. Huxley, H. E. (1969) The mechanism of muscular contraction. *Science 164*, 1356–1366.
2. Eisenberg, E., and Hill, T. L. (1985) Muscle contraction and free energy transduction in biological systems. *Science 227*, 999–1006.
3. Rayment, I., Rypniewski, W. R., Schmidt-Base, K., Smith, R., Tomchick, D. R., Benning, M. M., Winkelmann, D. A., Wesenberg, G., and Holden, H. M. (1993) Three-dimensional structure of myosin subfragment-1: A molecular motor. *Science 261*, 50–58.
4. Dominguez, R., Freyzon, Y., Trybus, K. M., and Cohen, C. (1998) Crystal structure of a vertebrate smooth muscle myosin motor domain and its complex with the essential light chain: Visualization of the pre-power stroke state. *Cell 94*, 559–571.
5. Bálint, M., Sréter, F. A., Wolf, I., Nagy, B., and Gergely, J. (1975) The substructure of heavy meromyosin. The effect of $Ca^{2+}$ and $Mg^{2+}$ on the tryptic fragmentation of heavy meromyosin. *J. Biol. Chem. 250*, 6168–6177.
6. Onishi, H., and Morales, M. F. (2007) A closer look at energy transduction in muscle. *Proc. Natl. Acad. Sci. U.S.A. 104*, 12714–12719.
7. Houdusse, A., and Cohen, C. (1996) Structure of the regulatory domain of scallop myosin at 2 Å resolution: Implications for regulation. *Structure 4*, 21–32.
8. Highsmith, S. (1999) Lever arm model of force generation by actin-myosin-ATP. *Biochemistry 38*, 9792–9797.
9. Milligan, R. A. (1996) Protein-protein interactions in the rigor actomyosin complex. *Proc. Natl. Acad. Sci. U.S.A. 93*, 21–26.
10. Rayment, I., Holden, H. M., Whittaker, M., Yohn, C. B., Lorenz, M., Holmes, K. C., and Milligan, R. A. (1993) Structure of the actin-myosin complex and its implications for muscle contraction. *Science 261*, 58–65.
11. Mendelson, R. A., and Morris, E. P. (1997) The structure of the acto-myosin subfragment 1 complex: Results of searches using data from electron microscopy and x-ray crystallography. *Proc. Natl. Acad. Sci. U.S.A. 94*, 8533–8538.
12. Root, D. D. (2002) A computational comparison of the atomic models of the actomyosin interface. *Cell Biochem. Biophys. 37*, 97–110.
13. Liu, Y., Scolari, M., Im, W., and Woo, H.-J. (2006) Protein-protein interactions in actin-myosin binding and structural effects of R405Q mutation: A molecular dynamics study. *Proteins: Struct., Funct., Bioinf. 64*, 156–166.
14. Murphy, C. T., and Spudich, J. A. (1999) The sequence of the myosin 50−20K loop affects myosin's affinity for actin throughout the actin-myosin ATPase cycle and its maximum ATPase activity. *Biochemistry 38*, 3785–3792.
15. Fujita, H., Sugiura, S., Momomura, S., Omata, M., Sugi, H., and Sutoh, K. (1997) Characterization of mutant myosins of *Dictyostelium discoideum* equivalent to human familial hypertrophic cardiomyopathy mutants. *J. Clin. Invest. 99*, 1010–1015.
16. Rovner, A. S., Freyzon, Y., and Trybus, K. M. (1995) Chimeric substitutions of the actin-binding loop activate dephosphorylated but not phosphorylated smooth muscle heavy meromyosin. *J. Biol. Chem. 270*, 30260–30263.
17. Ajtai, K., Garamszegi, S. P., Park, S., Velazquez Dones, A. L., and Burghardt, T. P. (2001) Structural characterization of $\beta$-cardiac myosin subfragment 1 in solution. *Biochemistry 40*, 12078–12093.
18. Bobkov, A. A., Bobkova, E. A., Lin, S. H., and Reisler, E. (1996) The role of surface loops (residues 204−216 and 627−646) in the motor function of the myosin head. *Proc. Natl. Acad. Sci. U.S.A. 93*, 2285–2289.
19. Mornet, D., Pantel, P., Audemard, E., and Kassab, R. (1979) The limited tryptic cleavage of chymotryptic S-1: An approach to the characterization of the actin site in myosin heads. *Biochem. Biophys. Res. Commun. 89*, 925–932.
20. Yamamoto, K., and Sekine, T. (1979) Interaction of myosin subfragment-1 with actin. III. Effect of cleavage of the heavy chain on its interaction with actin. *J. Biochem. 86*, 1869–1881.
21. Applegate, D., Azarcon, A., and Reisler, E. (1984) Tryptic cleavage and substructure of bovine cardiac myosin subfragment 1. *Biochemistry 23*, 6626–6630.
22. Coureux, P.-D., Wells, A. L., Menetrey, J., Yengo, C. M., Morris, C. A., Sweeney, H. L., and Houdusse, A. (2003) A structural state of the myosin V motor without bound nucleotide. *Nature 425*, 419–422.
23. Kollmar, M., Durrwang, U., Kliche, W., Manstein, D. J., and Kull, F. J. (2002) Crystal structure of the motor domain of a class-l myosin. *EMBO J. 21*, 2517–2525.
24. Rayment, I., Holden, H. M., Sellers, J. R., Fananapazir, L., and Epstein, N. D. (1995) Structural interpretation of the mutations in the $\beta$-cardiac myosin that have been implicated in familial hypertrophic cardiomyopathy. *Proc. Natl. Acad. Sci. U.S.A. 92*, 3864–3868.
25. Yamashita, H., Tyska, M. J., Warshaw, D. M., Lowey, S., and Trybus, K. M. (2000) Functional consequences of mutations in the smooth muscle myosin heavy chain at sites implicated in familial hypertrophic cardiomyopathy. *J. Biol. Chem. 275*, 28045–28052.
26. Lowey, S. (2002) Functional consequences of mutations in the myosin heavy chain at sites implicated in familial hypertrophic cardiomyopathy. *Trends Cardiovasc. Med. 12*, 348–354.
27. Lieto-Trivedi, A., Dash, S., and Coluccio, L. M. (2007) Myosin suface loop 4 modulates inhibition of actomyosin 1b ATPase activity by tropomyosin. *Biochemistry 46*, 2779–2786.
28. Gyimesi, M., Tsaturyan, A. K., Kellermayer, M. S. Z., and Malnasi-Csizmadia, A. (2008) Kinetic characterization of the function of myosin loop 4 in the actin-myosin interaction. *Biochemistry 47*, 283–291.
29. Burghardt, T. P., Hu, J. Y., and Ajtai, K. (2007) Myosin dynamics on the millisecond time scale. *Biophys. Chem. 131*, 15–28.
30. Birukov, G. K., Csortos, C., Marzilli, L., Dudek, S., Ma, S.-F., Bresnick, A. R., Verin, A. D., Cotter, R. J., and Garcia, J. G. N. (2001) Differential Regulation of Alternatively Spliced Endothelial Cell Myosin Light Chain Kinase Isoforms by p60Src. *J. Biol. Chem. 276*, 8567–8573.
31. Kojima, S., Fujiwara, K., and Onishi, H. (1999) SH1 (Cysteine 717) of smooth muscle myosin: Its role in motor function. *Biochemistry 38*, 11670–11676.
32. Onishi, H., Konishi, K., Fujiwara, K., Hayakawa, K., Tanokura, M., Martinez, H. M., and Morales, M. F. (2000) On the tryptophan residue of smooth muscle myosin that responds to binding of nucleotide. *Proc. Natl. Acad. Sci. U.S.A. 97*, 11203–11208.
33. Pardee, J. D., and Spudich, J. A. (1982) Purification of muscle actin. *Methods Enzymol. 85*, 164–179.
34. Fiske, C. H., and Subbarow, Y. (1925) The Colorimetric Determination of Phosphorus. *J. Biol. Chem. 66*, 375–400.
35. Ellison, P. A., DePew, Z. S., and Cremo, C. R. (2003) Both heads of tissue-derived smooth muscle heavy meromyosin bind to actin in the presence of ADP. *J. Biol. Chem. 278*, 4410–4415.
36. Kodama, T., Fukui, K., and Kometani, K. (1986) The initial phosphate burst in ATP hydrolysis by myosin and subfragment-1 as studied by a modified malachite green for determination of inorganic phosphate. *J. Biochem. 99*, 1465–1472.
37. Kouyama, T., and Mihashi, K. (1981) Fluorimetry study of *N*-(1-Pyrenyl)iodoacetamide-Labelled F-actin. Local structural change of actin protomer both on polymerization and on binding of heavy meromyosin. *Eur. J. Biochem. 114*, 33–38.
38. Ajtai, K., Garamszegi, S. P., Watanabe, S., Ikebe, M., and Burghardt, T. P. (2004) The myosin cardiac loop participates functionally in the actomyosin interaction. *J. Biol. Chem. 279*, 23415–23421.
39. Criddle, A. H., Geeves, M. A., and Jeffries, T. (1985) The use of actin labelled with *N*-(1-pyrenyl)iodoacetamide to study the interaction of actin with myosin subfragments and troponin/tropomyosin. *Biochem. J. 232*, 343–349.
40. Ohki, T., Mikhailenko, S. V., Morales, M. F., Onishi, H., and Mochizuki, N. (2004) Transmission of force and displacement within the myosin molecule. *Biochemistry 43*, 13707–13714.
41. Bing, W., Knott, A., Redwood, C., Esposito, G., Purcell, I., Watkins, H., and Marston, S. (2000) Effect of Hypertrophic Cardiomyopathy Mutations in Human Cardiac Muscle α-Tropomyosin (Asp175Asn and Glu180Gly) on the Regulatory Properties of Human Cardiac

Troponin Determined by in vitro Motility Assay. *J. Mol. Cell. Cardiol. 32*, 1489–1498.
42. Yount, R. G., Lawson, D., and Rayment, I. (1995) Is myosin a "back door" enzyme? *Biophys. J. 68*, 44s–49s.
43. Geeves, M. A., and Holmes, K. C. (1999) Structural mechanism of muscle contraction. *Annu. Rev. Biochem. 68*, 687–728.
44. Houdusse, A., Kalabokis, V. N., Himmel, D., Szent-Gyorgyi, A. G., and Cohen, C. (1999) Atomic structure of scallop myosin subfragment S1 complexed with MgADP: A novel conformation of the myosin head. *Cell 97*, 459–470.
45. Van Driest, S. L., Jaeger, M. A., Ommen, S. R., Will, M. L., Gersh, B. J., Tajik, A. J., and Ackerman, M. J. (2004) Comprehensive analysis of the $\beta$-myosin heavy chain gene in 389 unrelated patients with hypertrophic cardiomyopathy. *J. Am. Coll. Cardiol. 44*, 602–610.
46. Bagshaw, C. R., and Trentham, D. R. (1974) The characterization of myosin-product complexes and product-release steps during the magnesium ion-dependent adenosine triphosphate reaction. *Biochem. J. 141*, 331–349.
47. Hiratsuka, T. (1983) New ribose-modified fluorescent analogs of adenine and guanine nucleotides available as substrates for various enzymes. *Biochim. Biophys. Acta 742*, 496–508.
48. Nyitrai, M., Szent-Gyorgyi, A. G., and Geeves, M. A. (2002) A kinetic model of the co-operative binding of calcium and ADP to scallop (*Argopecten irradians*) heavy meromyosin. *Biochem. J. 365*, 19–30.
49. Onishi, H., Ohki, T., Mochizuki, N., and Morales, M. F. (2002) Early stages of energy transduction by myosin: Roles of Arg in Switch l, of Glue in Switch II, and of the salt-bridge between them. *Proc. Natl. Acad. Sci. U.S.A. 99*, 15339–15344.
50. Rosenfeld, S. S., Xing, J., Cheung, H. C., Brown, F., Kar, S., and Sweeney, H. L. (1998) Structural and kinetic studies of phosphorylation-dependent regulation in smooth muscle myosin. *J. Biol. Chem. 273*, 28682–28690.
51. Berger, C. E. M., Fagnant, P. M., Heizmann, S., Trybus, K. M., and Geeves, M. A. (2001) ADP Binding Induces an Asymmetry between the Heads of Unphosphorylated Myosin. *J. Biol. Chem. 276*, 23240–23245.
52. O'Connell, C. B., Tyska, M. J., and Mooseker, M. S. (2007) Myosin at work: Motor adaptations for a variety of cellular functions. *Biochim. Biophys. Acta 1773*, 615–630.
53. Bevington, P. R., and Robinson, D. K. (1992) Testing the Fit. In Data Reduction and Error Analysis for the Physical Sciences , pp 194−220, McGraw-Hill, New York.
54. Volkmann, N., Lui, H., Hazelwood, L., Trybus, K. M., Lowey, S., and Hanein, D. (2007) The R403Q myosin mutation implicated in familial hypertropic cardiomyopathy causes disorder at the actomyosin interface. *PLoS One,* No. e1123.
55. Lehman, W., Hatch, V., Korman, V., Rosol, M., Thomas, L., Maytum, R., Geeves, M. A., Van Eyk, J. E., Tobacman, L. S., and Craig, R. (2000) Tropomyosin and actin isoforms modulate the localization of tropomyosin strands on actin filaments. *J. Mol. Biol. 302*, 593–606.
56. Lockless, S. W., and Ranganathan, R. (1999) Evolutionarily conserved pathways of energetic connectivity in protein families. *Science 286*, 295–299.
57. Suel, G. M., Lockless, S. W., Wall, M. A., and Ranganathan, R. (2003) Evolutionarily conserved networks of residues mediate allosteric communication in proteins. *Nat. Struct. Mol. Biol. 10*, 59–69.
58. Tang, S., Liao, J. C., Dunn, A. R., Altman, R. B., Spudich, J. A., and Schmidt, J. P. (2007) Predicting allosteric communication in myosin via a pathway of conserved residues. *J. Mol. Biol. 373*, 1361–1373.